An Asymptotic and Numerical Investigation of Homogeneous Ignition in Catalytically Stabilized Channel Flow Combustion

JOHN MANTZARAS* and PETER BENZ

Paul Scherrer Institute, Combustion Research, CH-5232 Villigen-PSI, Switzerland

The gas-phase ignition of a fuel-lean premixed combustible gas is investigated in a forced convection two-dimensional laminar channel flow configuration established by two catalytically-active parallel plates placed at a distance $2b$ apart. The gaseous mixture has uniform inlet properties and both plate temperatures are constant and equal. First-order matched activation energy asymptotics are used to describe the reactive gaseous flow in conjunction with the boundary layer approximation, a one-step large activation energy gaseous reaction, and an infinitely fast (mass-transport-limited) catalytic reaction. A closed form ignition criterion is obtained for the gas-phase ignition distance in terms of nondimensional groups that are relevant to confined flows. The characteristic chemical and transverse diffusion time scales are included explicitly in the ignition criterion clearly demonstrating the competition between gaseous and catalytic fuel conversion while the effect of flow confinement (b) is included implicitly. The ignition criterion is valid over the range $0.002 < x/(bRePr) < 0.16$, with x the streamwise distance, Re the flow Reynolds number based on the channel halfwidth b and the uniform inlet properties, and Pr the Prandtl number. The temperature and transport parameter ranges of applicability are $1.5 < T_W/T_{IN} < 3$ (with T_W/T_{IN} the ratio of the catalytic wall to the inlet temperature) and $0.9 < Le < 2.0$ (with Le the Lewis number) respectively, rendering the ignition criterion of particular interest to hydrocarbon catalytically stabilized combustion (CST) applications. Numerical simulations are performed for channel flow catalytic combustion of a fuel-lean (equivalence ratio 0.32) propane–oxygen–nitrogen mixture using the same underlying chemistry assumptions as in the analytical asymptotic approach. The analytically calculated ignition distances are in good agreement with those numerically predicted. The effect of flow confinement (finite b) on gaseous ignition is examined by comparing ignition distances with the corresponding ones of the unconfined (flat plate) case. Flow confinement (decreasing b) increases the ignition distances due to the resulting increase in the channel surface-to-volume ratio. Moreover, the effect of flow confinement is important already from $x/(bRePr) = 0.002$.

NOMENCLATURE

A	parameter defined in Eq. 42
b	channel halfwidth
B	frequency factor in Arrhenius reaction of Eq. 7
$\tilde{B}$	function defined in Eq. 28
C_i	species concentration
c_p	specific heat at constant pressure
D_i	species diffusivity
Da	Damköhler number defined in Eq. 45
E	activation energy
f	nondimensional stream function defined in Eq. 13
F	function defined in Eq. 43
G_1	function defined after Eq. 30
G_2	function defined after Eq. 30
Le	Lewis number ($= Sc/Pr$)
n_i	reaction order, $i = F, O$
n	sum of reaction orders defined in Eq. 26
$Nu_{m,T}$	mean Nusselt number, constant wall temperature case
p	pressure
p^*	nondimensional pressure defined in Eq. 13
Pr	Prandtl number ($= c_p\mu/\lambda$)
q	heat of combustion per unit mass of fuel
Q_W	net wall heat flux defined in Eq. 48
$\tilde{Q}_W$	normalized net wall heat flux defined after Eq. 48
r	sign-determining exponent in Eqs. 9 and 19
R	universal gas constant
Re	Reynolds number defined in Eq. 12
s	dimensionless streamwise distance defined in Eq. 11
Sc	Schmidt number ($= \mu/\rho D$)
T	temperature
$\tilde{T}$	nondimensional temperature defined in Eq. 26
$\tilde{T}_a$	nondimensional activation energy defined in Eq. 26

*Corresponding author. E-mail: mantzaras@psi.ch

COMBUSTION AND FLAME 119:455–472 (1999)

Published by Elsevier Science Inc.

0010-2180/99/$–see front matter
PII S0010-2180(99)00071-1

u streamwise velocity
U_{IN} inlet streamwise velocity
v transverse velocity
W_i species molecular weight
$\bar{W}$ average mixture molecular weight
x streamwise physical coordinate
y transverse physical coordinate
Y_i species mass fraction
$\tilde{Y}_i$ normalized species mass fraction defined in Eq. 13
Z function defined after Eq. 30

Greek Symbols

α_{th} thermal diffusivity, $(\mu/\rho Pr)$
α parameter defined in Eq. B.7
β parameter defined in Eq. 26
γ reaction preexponential temperature dependence, Eq. 7
Δ_{cr} critical Damköhler number defined in Eq. 39
Δ^*_{cr} critical Damköhler number for ignition
ϵ small perturbation parameter defined in Eq. B.1
ζ nondimensional streamwise distance defined in Eq. 23
η nondimensional transverse coordinate defined in Eq. 11
η^* nondimensional transverse distance at the symmetry plane $(y = b)$
θ normalized temperature defined in Eq. 13
λ thermal conductivity
μ viscosity
ν_i species stoichiometric coefficient
ξ normalized transverse coordinate defined in Eq. 30
ρ density
τ_{ch} characteristic chemical time defined in Eq. 40
τ_{d} characteristic transverse diffusion time defined in Eq. 41
φ perturbation parameter for θ, Eq. 32
χ stretched transverse coordinate defined in Eq. 34
ψ stream function or species perturbation parameter Eq. B.4
ω_i species reaction rate
$\tilde{\omega}$ nondimensional reaction parameter defined in Eq. 29

Subscripts

F fuel
fr frozen
i index for species
ig ignition
IN inlet
inr inner solution
O oxidizer
P products
W wall
χ differentiation with respect to χ

Superscripts

$'$ differentiation with respect to η

INTRODUCTION

The combustion of fuel-lean gaseous premixtures with increased flame stability and very low NO_x emissions is an issue of prime interest in many practical applications, such as gas-fired turbines and burners. Catalytically stabilized thermal combustion (CST) is an alternative to the widely employed conventional lean premixed gaseous combustion. In CST partial—and less frequently, complete—fuel conversion is accomplished via heterogeneous (surface) oxidation reactions in burners with a suitably large surface-to-volume ratio. Complete fuel conversion is achieved with subsequent homogeneous (gaseous) combustion either in the catalytic burner itself or in a postcatalyst staged gaseous burner [1]. This process leads to substantial reduction of NO_x emissions as NO_x is produced almost exclusively from the gaseous reaction path [2, 3].

Catalytic combustors, such as the ones used in gas-fired turbines, are usually of the honeycomb type consisting of a multitude of catalytically active (Pt or Pd coated) tubular channels. The onset of homogeneous combustion in such a channel can be either intentional, whenever complete fuel conversion inside the channel is desired, or accidental, whenever the catalyst is not designed to cope with the ensuing gaseous heat release. In both cases, however, the homogeneous ignition and its precise location is an issue of great importance; in the former it determines the ratio of heterogeneous to homo-

geneous fuel conversion (and hence the NO_x emissions) and in the latter it can cause catalyst meltdown. Homogeneous ignition, although detrimental in many other industrial applications (such as the partial catalytic oxidation of methane to synthetic gas in a honeycomb monolith), is again of interest for safety reasons.

The homogeneous ignition in catalytic combustion has been investigated numerically in one-dimensional stagnation point flows [4–7], in two-dimensional external boundary layer flows [8–11], and in two-dimensional internal (channel) flows [12–16]. Stagnation point flows over catalytically active surfaces have provided an amenable platform to study the coupling between heterogeneous and homogeneous reactions. The regimes of homogeneous hydrocarbon combustion were identified [4, 5] using bifurcation theory and simplified chemistry for both the gaseous and surface kinetics. The homogeneous ignition of hydrogen–air mixtures was examined with detailed gaseous and simplified surface kinetics [6] and later with detailed gaseous and surface chemistries [7]; in these studies the coupling between gaseous and surface chemistries and the inhibition of the one path over the other was addressed. The two-dimensional studies included a simplified surface chemistry description and addressed the effect of radical adsorption–desorption reactions on gaseous combustion [8–12] and the influence of the controlling flow and chemical parameters on gaseous combustion [13, 14]. Recently [15] we investigated numerically the homogeneous ignition of lean methane–air mixtures in a channel flow using a two-dimensional elliptic model with detailed gaseous and surface chemistries; the key surface reactions affecting homogeneous ignition were identified. Homogeneous ignition distances predicted with this model were then successfully compared to measurements [16], thus strengthening the confidence on the CST applicability of newly developed surface reaction schemes [17].

Homogeneous ignition was also investigated analytically using matched activation energy asymptotics in external flows over catalytically active surfaces. Such studies included the ignition and extinction of a combustible gas in stagnation point flows [18–20], the ignition of a gas flowing over an isothermal [21] or nonisothermal [22] flat plate, and the ignition of a gas flowing over a cylindrical surface [23]. Notwithstanding the simplifications in the chemistry description, these studies have provided valuable information for the functional dependence of the ignition distance on the controlling flow, chemical, and transport parameters. Confined flow configurations, such as channel flows in catalytic honeycomb monoliths, are nevertheless of particular importance in practical applications and closed form solutions for the corresponding ignition distances have not been reported. In this article we undertake a theoretical study of homogeneous ignition in two-dimensional laminar channel CST flows with uniform inlet properties and isothermal catalytic surfaces. First-order matched activation energy asymptotics are employed along with a one-step large activation energy gaseous reaction and the boundary layer approximation for the reactive flow. A mass-transport-limited catalytic reaction is considered with fuel the deficient reactant. The main objective is to provide a closed form solution for the ignition distance in terms of nondimensional groups that are relevant to confined flows and based on chemical, flow, geometrical, and transport parameters. It is of particular interest to show the effect of flow confinement on the ignition distance. A numerical study of homogeneous ignition in channel CST is also performed (with the same underlying chemistry assumptions as in the analytical work) and the results are compared to the analytical predictions.

First, the mathematical model is given and the chemically frozen limit solution is presented in terms of the controlling parameters. The weakly reactive state is then formulated leading to the critical Damköhler numbers and the corresponding ignition distances. Application is made to channel CST of a propane–oxygen–nitrogen mixture with direct comparison between numerically and analytically predicted ignition distances and, finally, the functional dependence of the ignition distance on the controlling parameters of the problem is discussed.

MATHEMATICAL FORMULATION

The channel under investigation is formed by two parallel plates placed at a distance $2b$ apart

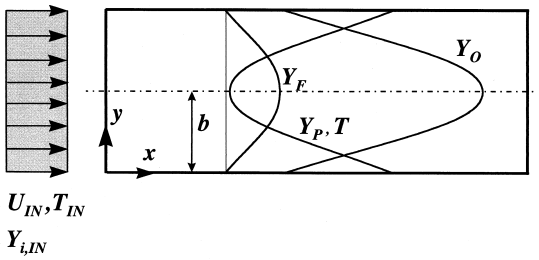

Fig. 1. Catalytic channel flow configuration. Typical profiles are of temperature (T), fuel (F), oxidizer (O), and product (P) mass fractions for a fuel-lean case and an infinitely fast catalytic reaction.

(Fig. 1). A fuel-lean gaseous premixture is admitted in the channel with uniform inlet axial velocity (U_{IN}) and temperature (T_{IN}) profiles. Both channel walls ($y = 0$ and $y = 2b$) are kept at a fixed temperature T_W. For gaseous combustion a single-step large activation energy irreversible Arrhenius reaction is considered, of the type

$$[F] + \nu_O[O] \rightarrow \nu_P[P]. \tag{1}$$

Catalytic fuel conversion proceeds according to the same global reaction, but with an infinitely fast rate (mass-transport-limited surface reaction). Typical species and temperature profiles before the onset of homogeneous combustion are illustrated in Fig. 1; the infinitely fast catalytic reaction drives the wall concentration of the limiting reactant (fuel) to zero. The governing equations are the continuity, momentum, energy, and species, which, under the boundary layer approximation are

$$\frac{\partial(\rho u)}{\partial x} + \frac{\partial(\rho v)}{\partial y} = 0 \tag{2}$$

$$\rho u \frac{\partial u}{\partial x} + \rho v \frac{\partial u}{\partial y} - \frac{\partial}{\partial y}\left(\mu \frac{\partial u}{\partial y}\right) = -\frac{dp}{dx} \tag{3}$$

$$\rho u c_p \frac{\partial T}{\partial x} + \rho u c_p \frac{\partial T}{\partial y} - \frac{\partial}{\partial y}\left(\lambda \frac{\partial T}{\partial y}\right) = q\omega_F \tag{4}$$

$$\rho u \frac{\partial Y_i}{\partial x} + \rho v \frac{\partial Y_i}{\partial y} - \frac{\partial}{\partial y}\left(\rho D_i \frac{\partial Y_i}{\partial y}\right) = -\omega_i \tag{5}$$

(the y-momentum being the trivial $\partial p/\partial y = 0$), supplemented with the ideal gas law

$$p = \rho \frac{R}{\overline{W}} T. \tag{6}$$

The fuel reaction rate is

$$\omega_F = W_F B T^{\gamma}\left(\frac{\rho Y_F}{W_F}\right)^{n_F}\left(\frac{\rho Y_O}{W_O}\right)^{n_O} \exp(-E/RT). \tag{7}$$

At the inlet ($x = 0$) uniform initial conditions are considered,

$$u = U_{IN},\ v = 0, \quad T = T_{IN},\ p = p_{IN},\ Y_i = Y_{i,IN}. \tag{8}$$

The wall ($x > 0$, $y = 0$) boundary conditions are

$$u = v = 0, \quad T = T_W,$$

$$Y_F = 0,\ \frac{\partial Y_i}{\partial y} = (-1)^r\left(\frac{D_F}{D_i}\right)\left(\frac{W_i \nu_i}{W_F}\right)\frac{\partial Y_F}{\partial y} \tag{9}$$

$i \neq F$, $r = 0$ for the oxidizer, $r = 1$ for the products.

Finally, at the plane of symmetry ($x > 0, y = b$) the boundary conditions are

$$\frac{\partial u}{\partial y} = v = 0, \qquad \frac{\partial T}{\partial y} = 0, \qquad \frac{\partial Y_i}{\partial y} = 0. \tag{10}$$

For confined flows it is appropriate to introduce the nondimensional independent variables

$$s = x/(bRe) \text{ and } \eta = \frac{1}{b\rho_{IN}\sqrt{2s}}\int_0^y \rho\, dy \tag{11}$$

with Re the flow Reynolds number based on the channel halfwidth and the uniform inlet properties,

$$Re = \frac{\rho_{IN} U_{IN} b}{\mu_{IN}}. \tag{12}$$

Introducing the stream function $\psi(x, y)$ such that $\partial\psi/\partial x = -\rho v$ and $\partial\psi/\partial y = \rho u$ and the nondimensional variables

$$f = \frac{\psi}{b\rho_{IN}U_{IN}\sqrt{2s}},\ p^* = \frac{p}{\rho_{IN}U_{IN}^2},$$

$$\theta = \frac{T_W - T}{T_W - T_{IN}},\ \tilde{Y}_i = \left(\frac{W_F}{\nu_i W_i}\right)Y_i \tag{13}$$

and further assuming equal species diffusivities D_i, constant values for c_p, $\rho\mu$, $\rho\lambda$, and $\rho^2 D_i$ (resulting in constant Prandtl and Schmidt num-

bers, Pr and Sc respectively), the governing equations 2–6 become

$$\frac{\partial^3 f}{\partial \eta^3} + f\frac{\partial^2 f}{\partial \eta^2} + 2s\left(\frac{\partial f}{\partial s}\right)\frac{\partial^2 f}{\partial \eta^2} - 2s\left(\frac{\partial f}{\partial \eta}\right)\frac{\partial^2 f}{\partial \eta \partial s} = 2s\left(\frac{\rho_{IN}}{\rho}\right)\left(\frac{dp^*}{ds}\right) \tag{14}$$

$$Pr^{-1}\frac{\partial^2 \theta}{\partial \eta^2} + f\frac{\partial \theta}{\partial \eta} + 2s\left(\frac{\partial f}{\partial s}\right)\frac{\partial \theta}{\partial \eta} - 2s\left(\frac{\partial f}{\partial \eta}\right)\frac{\partial \theta}{\partial s} = 2s\,\frac{Rebq}{U_{IN}c_p(T_W - T_{IN})}\left(\frac{\omega_F}{\rho}\right) \tag{15}$$

$$Sc^{-1}\frac{\partial^2 \tilde{Y}_i}{\partial \eta^2} + f\frac{\partial \tilde{Y}_i}{\partial \eta} + 2s\left(\frac{\partial f}{\partial s}\right)\frac{\partial \tilde{Y}_i}{\partial \eta} - 2s\left(\frac{\partial f}{\partial \eta}\right)\frac{\partial \tilde{Y}_i}{\partial s} = 2s\,\frac{Reb}{U_{IN}}\left(\frac{\omega_F}{\rho}\right) \tag{16}$$

$$p = \rho\,\frac{R}{\bar{W}}\,[T_W - \theta(T_W - T_{IN})] \tag{17}$$

with initial conditions ($s = 0$)

$$f' = 1,\ \theta = 1,\ p^* = p^*_{IN},\ \tilde{Y}_i = \tilde{Y}_{i,IN}, \tag{18}$$

wall boundary conditions ($s > 0,\ \eta = 0$)

$$f = 0,\ f' = 0,\ \theta = 0,\ \tilde{Y}_i = (-1)^r(\tilde{Y}_{i,IN} - \tilde{Y}_{F,IN}) \tag{19}$$

$r = 0$ for the reactants and $r = 1$ for the products,

and plane-of-symmetry ($s > 0,\ \eta = \eta^*$) boundary conditions

$$f'' = 0,\ \theta' = 0,\ \tilde{Y}_i' = 0. \tag{20}$$

The species wall boundary conditions in Eq. 19 indicate a stoichiometric product composition at the surface, a direct outcome of the equal mass diffusivities assumption. They are equivalent to the corresponding boundary conditions of Eq. 9 when D_i are equal. It is noted that in the numerical solution of Eqs. 14–17 (discussed in the next section) the species wall boundary conditions of Eq. 9 are used. They, of course, lead (for equal D_i) to the wall mass fractions of Eq. 19. The formulation of Eq. 19 is preferred for the ensuing asymptotic analysis.

ASYMPTOTIC ANALYSIS

Chemically Frozen Limit

Within the context of a large activation energy reaction, prior to ignition the gas phase is considered to be chemically frozen ($E/RT_W \to \infty$) and fuel is consumed only via the surface reaction path. The energy and species conservation Eqs. 15 and 16 become,

$$Pr^{-1}\frac{\partial^2 \theta}{\partial \eta^2} + f\frac{\partial \theta}{\partial \eta} + 2s\left(\frac{\partial f}{\partial s}\right)\frac{\partial \theta}{\partial \eta} - 2s\left(\frac{\partial f}{\partial \eta}\right)\frac{\partial \theta}{\partial s} = 0 \tag{21}$$

$$Sc^{-1}\frac{\partial^2 \tilde{Y}_i}{\partial \eta^2} + f\frac{\partial \tilde{Y}_i}{\partial \eta} + 2s\left(\frac{\partial f}{\partial s}\right)\frac{\partial \tilde{Y}_i}{\partial \eta} - 2s\left(\frac{\partial f}{\partial \eta}\right)\frac{\partial \tilde{Y}_i}{\partial s} = 0. \tag{22}$$

The chemically frozen state is described by Eqs. 14, 21, 22, and 17 with the initial and boundary conditions 18–20. The problem under consideration is that of heat and mass transfer in the hydrodynamically and thermally developing section of a channel with variable fluid properties. Analytical solutions in terms of series expansions have been presented for the constant fluid property problem by linearizing the Navier-Stokes equations; for the hydrodynamic problem itself by Langhaar [24], Han [25], and Sparrow et al. [26], and for the hydrodynamic problem with mass transfer through the walls by Williams [27].

The governing set of equations is intrinsically nonsimilar and is solved numerically. The details of the numerical solution are presented in Appendix A. Computed transverse profiles of temperature, velocity, and species mass fractions are illustrated in Fig. 2 for a propane–oxygen–nitrogen mixture with inlet mass fractions $Y_{C3H8} = 0.0332$, $Y_{O2} = 0.3764$ (equivalence ratio $\varphi = 0.32$), and $Y_{N2} = 0.5904$ respectively, $b = 1.5$ mm, $U_{IN} = 8$ m/s, $p_{IN} = 1$ bar, $T_{IN} = 600$ K, $T_W = 1200$ K, $Pr = 0.7$, $Sc = 1.28$, and $c_p = 1.29$ kJ/kgK. The catalytic one-step reaction is $C_3H_8 + 5O_2 \to 3CO_2 + 4H_2O$.

For the assessment of gaseous ignition the essential parts of the chemically frozen solution are the local transverse wall gradients of tem-

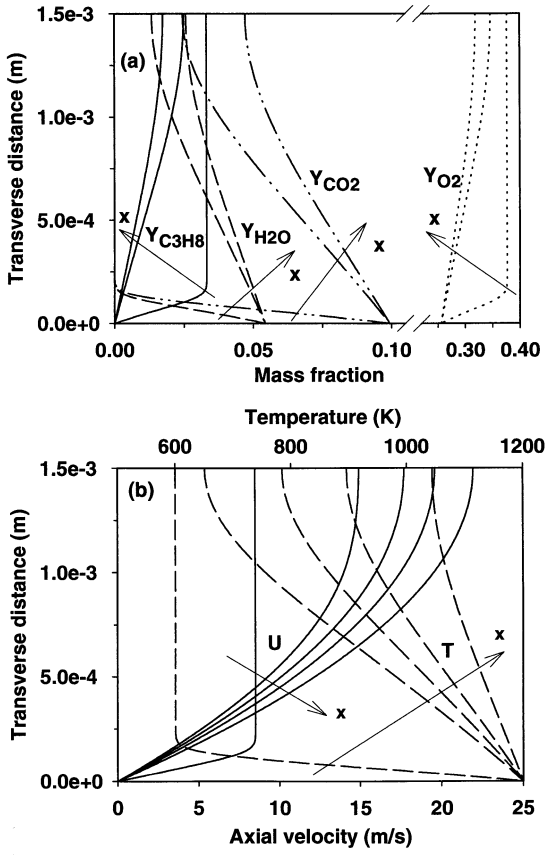

Fig. 2. Chemically frozen limit solution for fuel-lean (equivalence ratio 0.32) propane–oxygen–nitrogen mixture, U_{IN} = 8 m/s, T_{IN} = 600 K, T_W = 1200 K, and b = 1.5 mm; (a) Transverse profiles of C_3H_8 (solid lines), H_2O (dashed lines), CO_2 (dotted-dashed lines), and O_2 (dotted lines) mass fractions at streamwise distances x = 0.015, 7.20, and 11.94 cm. The wall is at y = 0. Arrows indicate the direction of increasing x. (b) Transverse profiles of axial velocity (solid lines) and temperature (dashed lines) at streamwise distances x = 0.015, 2.40, 4.78, 7.20, and 11.94 cm.

perature, $\theta'_{fr,W}$, and fuel mass fraction, $(\tilde{Y}'_F)_{fr,W}$. This will become apparent in the next section where the weakly reactive state is formulated. Closed form solutions are presented below for these gradients in terms of the relevant geometrical, flow, and transport parameters. Inspection of the governing equations reveals that the chemically frozen state is a function of the independent variables s and η, the Pr and Sc numbers, and the ratio T_W/T_{IN}. When discussing the local wall temperature gradient it is convenient to define a new streamwise coordinate,

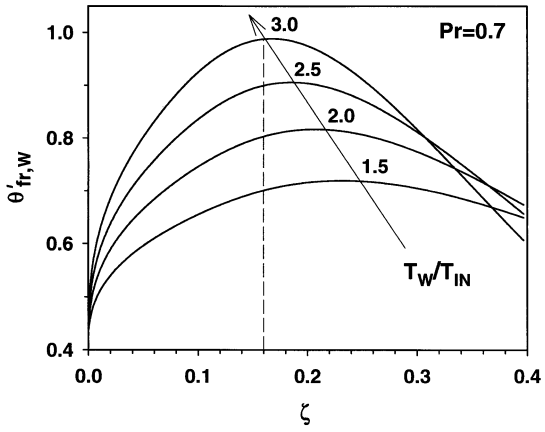

Fig. 3. Chemically frozen solution; computed streamwise profiles of nondimensional transverse wall temperature gradient for four values of T_W/T_{IN}.

$$\zeta = \frac{x}{bRePr} = \frac{s}{Pr} \tag{23}$$

relevant for heat transfer in confined flows [29]. The plot of $\theta'_{fr,W}$ versus ζ is presented in Fig. 3 for a fixed Pr = 0.7 and parameter the ratio T_W/T_{IN}. Extensive computations were carried out by varying U_{IN} (0.5 to 30 m/s), b (0.2 to 40 mm), T_{IN} (300 to 800 K), p_{IN} (1 to 15 bars), T_W (450 to 2400 K), Sc (0.4 to 1.5) and the results fall on the curves of Fig. 3, clearly showing that $\theta'_{fr,W}$ depends on ζ, Pr, and T_W/T_{IN}. There is an additional mild dependence on equivalence ratio for nonequimolar reactions. The computations in Fig. 3 pertain to lean methane–air mixtures with equivalence ratio ranging from 0.1 to 0.6. Methane burns equimolarly ($CH_4 + 2O_2 \rightarrow CO_2 + 2H_2O$), thus preserving the mean molecular weight $\bar{W}$. In nonequimolar reactions the ratio ρ_{IN}/ρ appearing in Eq. 14 is also a function of $\bar{W}$; Eq. 17 yields $\rho_{IN}/\rho = (p_{IN}/p)(\bar{W}_{IN}/\bar{W})[T_W/T_{IN} - \theta(T_W/T_{IN} - 1)]$ and given the fact that for streamwise distances $\zeta <$ 0.4 the pressure drop is small so that $p_{IN}/p \approx 1$, ρ_{IN}/ρ becomes a function of θ, T_W/T_{IN}, and $\bar{W}_{IN}/\bar{W}$ (and hence equivalence ratio). For hydrocarbon combustion with a global reaction $C_nH_m + (n + m/4)O_2 \rightarrow nCO_2 + (m/2)H_2O$, however, and in particular for lean fuel–air applications the change in $\bar{W}$ is small and the family of curves presented in Fig. 3 is virtually unaffected by equivalence ratio variation. Only in reactions with a strong volume change, for

example CO + ½ $O_2 \rightarrow CO_2$, can such an effect be observed. Even then, for CO–air combustion, there is only a maximum of 2% deviation for each family of curves in Fig. 3 for equivalence ratios ranging between 0.1 and 0.4. Hence, the equivalence ratio effect was not considered. The profiles of Fig. 3 pass through a maximum and drop as the mixture bulk temperature approaches T_W. Moreover, the profile maxima are displaced to shorter ζ for larger T_W/T_{IN}. To facilitate the desired parametric description we consider $\zeta < 0.16$, a range where all curves of Fig. 3 are monotonically increasing with ζ. The following parametric dependence is then suggested for $\theta'_{fr,W}$:

$$\theta'_{fr,W} = (0.43 + 0.45\zeta^{0.35})\, Pr^{1/3+0.242\zeta^{0.2}} \left(\frac{T_W}{T_{IN}}\right)^{0.774\zeta^{0.2}} \qquad (24)$$

valid for $0.002 < \zeta < 0.16$ and $1.5 < T_W/T_{IN} < 3.0$. It must be stated that although accurate numerical predictions can be obtained for $\zeta < 0.002$, the parametric description over the entire ζ-range can be accomplished only with complicated, piece-wise continuous functions. In any case, the distance $\zeta = 0.002$ is, in most CST applications, a fraction of the channel hydraulic diameter.

The wall gradient $\theta'_{fr,W}$ is plotted versus ζ in Fig. 4 over the streamwise range of interest. The agreement between the computations (solid lines) and the proposed dependence of Eq. 24 (dotted lines) is better than 1.6% over the entire range $0.002 < \zeta < 0.16$. Although $Pr = 0.7$ is a good estimate for most lean hydrocarbon combustion applications, parametric studies with Pr in the range 0.6 to 1.0 are in excellent agreement with the power law dependence $Pr^{1/3+0.242\zeta^{0.2}}$ of Eq. 24. This is also shown in the insert of Fig. 4 where the ratio $R_\theta = (\theta'_{fr,W})_{Pr}/(\theta'_{fr,W})_{Pr=0.7}$ is presented for three different Pr numbers; R_θ is independent of T_W/T_{IN} and the agreement between the computations (solid lines) and the Prandtl number power law dependence (dotted lines) is better than 0.4%.

Apart from the very good fit to the numerical predictions, Eq. 24 carries the proper functional dependencies. This can be seen by taking the flat plate limit ($\zeta \rightarrow 0$). Although Eq. 24 is

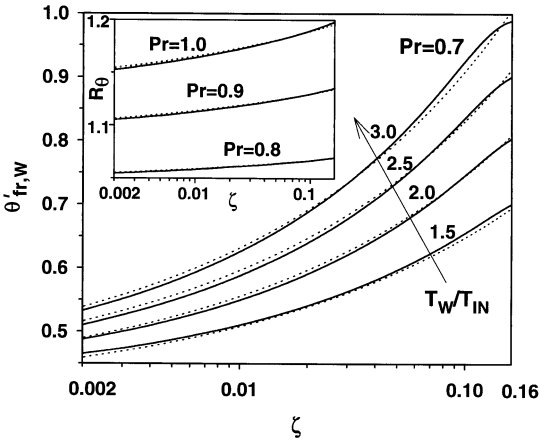

Fig. 4. Chemically frozen solution. Streamwise profiles of nondimensional transverse wall temperature gradient $\theta'_{fr,W}$ for four values of T_W/T_{IN}. Computations (solid lines) and predictions from Eq. 24 (dotted lines). In the insert figure the effect of Prandtl number on $\theta'_{fr,W}$ is illustrated with streamwise plots of the ratio $R_\theta = (\theta'_{fr,W})_{Pr}/(\theta'_{fr,W})_{Pr=0.7}$; solid lines are computations and dotted lines are the power-law Prandtl number dependence of Eq. 24.

accurate for $\zeta > 0.002$, extrapolation to $\zeta = 0$ yields $\theta'_{fr,W} = 0.43\, Pr^{1/3}$, in agreement with the flat plate solution which, to a good approximation for order unity Prandtl numbers, is [30] $\theta''_{fr,W} = f''(0) Pr^{1/3}$, with $f''(0) = 0.4696$, the solution of the Blasius flat plate similarity equation $f''' + ff'' = 0$ [31]. Note also that T_W/T_{IN} is not a relevant parameter for the flat plate problem, which is also captured by Eq. 24. Finally, Nusselt numbers have been calculated and compared to literature data. For the hydrodynamically and thermally developing flow between two parallel isothermal plates, Nusselt numbers have been computed for the constant fluid property case by Hwang [32]. The constant property solution should be approached as $T_W/T_{IN} \rightarrow 1$. In Fig. 5 the computed mean Nusselt number $Nu_{m,T}$ (the Nusselt number is based on $4b$, the channel hydraulic diameter) is plotted for a case with $T_{IN} = 600$ K, $Re = 500$, $Pr = 0.72$ and four values of T_W/T_{IN}. The constant property solution [32] is in quite good agreement with the $T_W/T_{IN} = 1.04$ computations.

The local fuel transverse wall gradient is now calculated. The variables θ and $(1/\tilde{Y}_{F,IN})\tilde{Y}_F$ have the same initial and boundary conditions and their profiles are identical for $Pr = Sc$. Transverse fuel wall gradients $(1/\tilde{Y}_{F,IN})(\tilde{Y}'_F)_{fr,W}$

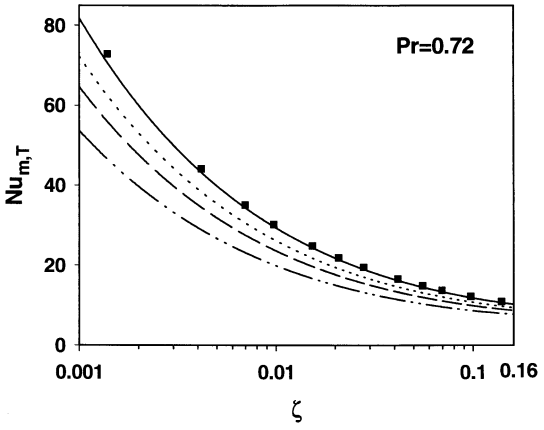

Fig. 5. Computed streamwise profiles of mean Nusselt number for $Pr = 0.72$, $Re = 500$, $T_{IN} = 600$ K; $T_W/T_{IN} = 1.04$ (solid lines), 1.19 (dotted lines), 1.34 (dashed lines), and 1.64 (dashed-dotted lines). Symbols are the constant property solution from [32].

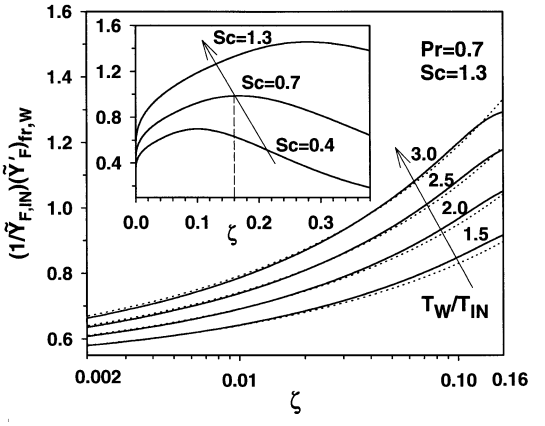

Fig. 6. Chemically frozen limit. Streamwise profiles of nondimensional fuel transverse wall gradient for $Pr = 0.7$ and $Sc = 1.3$, with parameter the ratio T_W/T_{IN}; computations (solid lines) and predictions (dotted lines) from Eq. 25. In insert figure, streamwise profiles of nondimensional transverse fuel wall gradient are presented for three Schmidt numbers and $T_W/T_{IN} = 3.0$.

are plotted versus ζ in the insert of Fig. 6 for three different Schmidt numbers, $Sc = 0.4$, 0.7, and 1.3 respectively and a fixed ratio $T_W/T_{IN} = 3$. The $Sc = 0.7$ curve coincides with the $T_W/T_{IN} = 3$ temperature wall gradient curve of Fig. 3. Fuel depletion is faster for smaller Sc resulting in a displacement of the profile maxima to shorter ζ for smaller Sc. To maintain a monotonic dependence of $(1/\tilde{Y}_{F,IN})(\tilde{Y}'_F)_{fr,W}$ with ζ (an essential feature for the parametric description of the solution) up to the streamwise distance of interest $\zeta = 0.16$, it is required that $Sc > Pr$, i.e., $Le > 1$. It is preferable to present the proposed transverse fuel wall gradient parametric dependence in terms of its ratio to the temperature wall gradient:

$$\frac{(1/\tilde{Y}_{F,IN})(\tilde{Y}'_F)_{fr,W}}{\theta'_{fr,W}} = Le^{1/3+0.19\zeta^{0.35}} \tag{25}$$

valid for $0.002 < \zeta < 0.16$ and $1.5 < T_W/T_{IN} < 3.0$. Computed fuel wall gradient profiles are plotted with solid lines in Fig. 6 for $Pr = 0.7$, $Sc = 1.3$, and the ratio T_W/T_{IN}. The dotted lines in the same figure are the corresponding profiles calculated from Eq. 25 and the computed $\theta'_{fr,W}$ profiles of Fig. 3. The agreement is better than 2.5%, and this is also the case for Sc numbers up to 1.4 ($Le = 2.0$). Equation 25 also can be extended to Le numbers slightly less than unity, so that it is applicable over the range $0.9 < Le < 2.0$ with accuracy better than 2.5%.

Finally, suffice it to say that the flat plate limit ($\zeta \to 0$) of Eq. 25 gives a $Le^{1/3}$ dependence for the transverse wall gradient ratio, in agreement with [30] for order unity Pr and Sc numbers.

The temperature range $1.5 < T_W/T_{IN} < 3.0$ in the parametric studies of Eqs. 24 and 25 is sufficient for most CST applications. For hydrocarbon CST the incoming mixture is preheated typically to 500–700 K and the wall temperature rarely exceeds 1500 K because of substrate and catalyst thermal stability considerations [12–16]. In addition, the range $0.002 < \zeta < 0.16$ covers a significant length in a typical honeycomb channel, particularly at high pressure operations where the Reynolds number is large. For example, in a honeycomb channel with a 1 mm × 1 mm square cross section, $T_{IN} = 600$ K, $U_{IN} = 15$ m/s, and a pressure of 15 bars typical for gas turbines, the equivalent parallel plate configuration has a halfwidth $b = 0.25$ mm (so that the hydraulic diameter is the same in both cases) resulting in a Re of about 1100; in this case the nondimensional distance $\zeta = 0.16$ corresponds, for $Pr = 0.7$, to a physical distance $x = 123b$. More important than the physical distance x is, in practical applications, the catalytic fuel conversion: the computations show that at $\zeta = 0.16$ the catalytic fuel conversion ranges from 31.2% ($T_W/T_{IN} = 1.5$) to 41.6% ($T_W/T_{IN} = 3$). Given the fact that new hybrid CST designs [1]

employ a sequence of two or three catalytic honeycomb sections followed by a homogeneous combustion zone, it is likely that the fuel conversion in each individual catalytic section does not exceed the above stated numbers. Finally, the transport parameter range $0.9 < Le < 2.0$ covers a large number of fuel-lean hydrocarbon combustion applications.

Weakly Reactive State

Equations 14–20 define the weakly reactive state. Introducing the nondimensional variables

$$\tilde{T} = \frac{c_p T}{q}, \quad \tilde{T}_a = \frac{E}{RT_W}, \tag{26}$$

$$\beta = \frac{\tilde{T}_W - \tilde{T}_{IN}}{\tilde{T}_W}, \quad n = n_O + n_F, \tag{26}$$

the energy equation (Eq. 15) becomes

$$Pr^{-1}\frac{\partial^2\theta}{\partial\eta^2} + f\frac{\partial\theta}{\partial\eta} + 2s\left(\frac{\partial f}{\partial s}\right)\frac{\partial\theta}{\partial\eta} - 2s\left(\frac{\partial f}{\partial\eta}\right)\frac{\partial\theta}{\partial s} = \frac{2s\tilde{B}\tilde{\omega}}{\beta\tilde{T}_W} \tag{27}$$

with

$$\tilde{B} = B\left(\frac{Reb}{U_{IN}}\right)\left(\frac{p\bar{W}}{RW_F}\right)^{n-1}\nu_O^{n_O}\left(\frac{q}{c_p}\right)^{1+\gamma-n}\tilde{T}_W^{1+\gamma-n} \tag{28}$$

and

$$\tilde{\omega} = (1-\beta\theta)^{1+\gamma-n}\tilde{Y}_F^{n_F}\tilde{Y}_O^{n_O}\exp\left(\frac{-\tilde{T}_a}{1-\beta\theta}\right). \tag{29}$$

A new transverse normalized coordinate ξ is introduced,

$$\xi = \frac{\displaystyle\int_0^{\eta}\exp\left[-Pr\int_0^{\eta} f\,d\eta\right]d\eta}{\displaystyle\int_0^{\eta^*}\exp\left[-Pr\int_0^{\eta} f\,d\eta\right]d\eta} = \frac{Z(\eta)}{Z(\eta^*)} \tag{30}$$

with $Z(\eta) = \int_0^{\eta}\exp[-Pr\int_0^{\eta} f\,d\eta]\,d\eta$ and $Z(\eta^*) = \int_0^{\eta^*}\exp[-Pr\int_0^{\eta} f\,d\eta]\,d\eta$. Defining $G_1 = dZ/d\eta$, $G_2 = Z(\eta^*)$ and recognizing that $d\xi = G_1/G_2\,d\eta$, Eq. 27 becomes

$$Pr^{-1}\frac{\partial^2\theta}{\partial\xi^2} = 2s\left(\frac{G_2}{G_1}\right)\left[\frac{G_2}{G_1}(f')\frac{\partial\theta}{\partial s} - \left(\frac{\partial f}{\partial s}\right)\frac{\partial\theta}{\partial\xi}\right] + 2s\frac{G_2^2}{G_1^2}\frac{\tilde{B}\tilde{\omega}}{\beta\tilde{T}_W} \tag{31}$$

with boundary conditions

$$\theta = 0 \text{ at } \xi = 0 \text{ and } \frac{\partial\theta}{\partial\xi} = 0 \text{ at } \xi = 1.$$

As the combustible mixture approaches ignition, the species and temperature profiles will be perturbed from the corresponding frozen limit profiles by a small quantity of order ϵ. For the region which is close to the high temperature wall (inner zone), a first-order expansion about the chemically frozen solution yields,

$$\theta_{inr} = \theta_{fr} - \epsilon\varphi \tag{32}$$

with φ the corresponding perturbation. The negative sign denotes a decrease in θ with increasing temperature according to the definition of Eq. 13. For the chemically frozen temperature solution, a Taylor series expansion near the wall ($\eta \to 0$) yields $\theta_{fr} = \theta_W + \theta'_{fr,W}\eta + O(\eta^2)$, and since θ_W is zero

$$\theta_{fr} = \theta'_{fr,W}\eta. \tag{33}$$

The connection between ξ and η as $\eta \to 0$ is deduced from Eq. 30 considering the corresponding Taylor series expansion for the normalized stream function; $f = f''_W\eta^2/2$ due to the wall boundary conditions of Eq. 19. Substituting the last expression in Eq. 30 yields $\xi = \eta/G_2$ and hence Eq. 33 becomes $\theta_{fr} = \theta'_{fr,W}\xi G_2$. A new stretched transverse coordinate χ is further introduced,

$$\theta'_{fr,W}\xi G_2 = \epsilon\chi. \tag{34}$$

The last expression, along with Eqs. 32 and 33, gives for the inner expansion of temperature

$$\theta_{inr} = \epsilon(\chi - \varphi). \tag{35}$$

Equation 35 is further substituted in Eq. 31 and the leading term in ϵ balancing the reaction term is sought. This is because in the inner zone the reaction term must be important. Neglecting the $O(\epsilon)$ and $O(\epsilon^3)$ contributions with respect to the order unity diffusion term, the

following differential equation for the perturbation quantity φ is obtained,

$$\frac{d^2\varphi}{d\chi^2} = -\frac{\epsilon Pr 2s\tilde{B}\tilde{\omega}}{G_1^2(\theta'_{fr,W})^2\beta\tilde{T}_W} \tag{36}$$

with boundary conditions $\varphi(0) = 0$ and $\partial\varphi/\partial\chi = 0$ at $\chi \to \infty$. The second boundary condition is obtained via matching with the outer solution, a procedure similar to that described in Law and Law [33] and hence not repeated here.

The variables G_1 and $\tilde{\omega}$ appearing in Eq. 36 are calculated for the inner zone. This requires additional expansions for the species inner profiles similar to that of the temperature (Eq. 32). The details are provided in Appendix B, leading to the final equation describing the perturbation quantity φ

$$\frac{d^2\varphi}{d\chi^2} = -\Delta_{cr}(\chi - \alpha\varphi)^{n_F}\exp(\varphi - \chi) \tag{37}$$

$$\varphi(0) = 0 \text{ and } \left.\frac{\partial\varphi}{\partial\chi}\right|_{\chi\to\infty} = 0 \tag{38}$$

with α defined in Eq. B.7 and Δ_{cr} the critical Damköhler number,

$$\Delta_{cr} = 2s\left[B\left(\frac{p\bar{W}}{R}\right)^{n-1}\left(\frac{W_F^{1-n_F}}{W_O^{n_O}}\right)T_W^{1+\gamma-n}\left(Y_{O,IN} - \frac{W_O\nu_O}{W_F}Y_{F,IN}\right)^{n_O}Y_{F,IN}^{n_F}\exp\left(-\frac{E}{RT_W}\right)\right]\left[\frac{bRePr}{U_{IN}}\right]$$
$$\cdot\left[\frac{T_W^{2(1+n_F)}\left(\frac{R}{E}\right)^{1+n_F}\left(\frac{q}{c_p}\right)}{(T_W - T_{IN})^{2+n_F}}\right]\left[\left(\frac{(1/\tilde{Y}_{F,IN})(\tilde{Y}'_F)_{fr,W}}{\theta'_{fr,W}}\right)^{n_F}\frac{1}{(\theta'_{fr,W})^2}\right]. \tag{39}$$

RESULTS AND DISCUSSION

Ignition Distances

The ignition distance s_{ig} is deduced from Eq. 39 once the critical Damköhler number for ignition, Δ^*_{cr}, has been determined. The first bracket in Eq. 39 is a characteristic inverse chemical time scale evaluated at the wall temperature and inlet species concentrations,

$$\tau_{ch} = \left[B\left(\frac{p\bar{W}}{R}\right)^{n-1}\left(\frac{W_F^{1-n_F}}{W_O^{n_O}}\right)T_W^{1+\gamma-n}\left(Y_{O,IN} - \frac{W_O\nu_O}{W_F}Y_{F,IN}\right)^{n_O}Y_{F,IN}^{n_F}\exp\left(-\frac{E}{RT_W}\right)\right]^{-1} \tag{40}$$

The second bracket in Eq. 39 with the definitions of Re and Pr becomes $b^2/\alpha_{th,IN}$, which is a characteristic transverse diffusion time scale,

$$\tau_d = bRePr/U_{IN} = b^2/\alpha_{th,IN}. \tag{41}$$

The third bracket in Eq. 39 is a nondimensional quantity involving the temperatures T_W and T_{IN} as well as the exothermicity (q) and reactivity (E) of the gaseous reaction. The inverse of this term is defined as,

$$A = \left[\frac{(T_W - T_{IN})^{2+n_F}}{T_W^{2(1+n_F)}\left(\frac{R}{E}\right)^{1+n_F}\left(\frac{q}{c_p}\right)}\right]. \tag{42}$$

Finally, the fourth bracket in Eq. 39 involves the chemically frozen state wall gradients of Eqs. 24 and 25. We define the function F,

$$F(\zeta) = \frac{Le^{n_F(1/3+0.19\zeta^{0.35})}}{\left[(0.43 + 0.45\zeta^{0.35})Pr^{1/3+0.242\zeta^{0.2}}\left(\frac{T_W}{T_{IN}}\right)^{0.774\zeta^{0.2}}\right]^2}. \tag{43}$$

Solving Eq. 39 for s and using Eqs. 23–25 and 39–43, the nondimensional ignition distance (expressed in ζ rather than s) becomes,

$$\zeta_{ig}\frac{F(\zeta_{ig})}{\Delta^*_{cr}(\zeta_{ig})} = \frac{1}{2Pr}A\frac{1}{Da} \tag{44}$$

with Da the characteristic Damköhler number of the problem,

$$Da = \tau_d/\tau_{ch}. \tag{45}$$

Equation 44 is implicit in ζ_{ig} and is solved iteratively. The dependence of the critical

Damköhler number on ζ is due to the ζ-dependence of the parameter α (see Eq. B.7) through the wall gradient ratio of Eq. 25; this dependence is nevertheless weak as it results in a maximum 6% change in α for $0.002 < \zeta < 0.16$ and $Le = 2$. The influence of the various parameters on the ignition distance is discussed with the aid of Eq. 44. The dependence on the Damköhler number Da (and hence on the characteristic chemical and diffusion times) is explicit. The left-hand side of Eq. 44, as will be discussed in the forthcoming Fig. 8, is a monotonically increasing function of ζ. This results in an increase of the ignition distance with decreasing Da. The characteristic chemical and diffusion time scales appearing in Da demonstrate the competition between surface and gaseous reactions; short diffusion times favor fast catalytic fuel depletion and therefore inhibit gaseous ignition, while short chemical times favor the onset of gaseous ignition. The flow confinement (b) is included in the diffusion time scale, but also implicitly in the left-hand side of Eq. 44 through the function $F(\zeta)$. The temperature and fuel wall gradients appearing in $F(\zeta)$ carry the effects of flow acceleration and fuel depletion along the streamwise direction and hence they are a particular feature of the confined flow configuration. It must be stated that the ignition criterion of Eq. 44 provides no information for the possibility of homogeneous ignition when $\zeta_{ig} > 0.16$. However, when $\zeta_{ig} < 0.002$ homogeneous ignition is always guaranteed, although the ignition distance deduced from Eq. 44 will not be as accurate.

An application of Eq. 44 is presented next. We consider first-order reactions with respect to fuel ($n_F = 1$). The first step is to determine Δ^*_{cr} by solving Eq. 37. The critical ignition Damköhler number Δ^*_{cr} defines a turning point in the perturbation wall gradient $\varphi_\chi(0)$ versus Δ_{cr} curve, corresponding to a typical thermal runaway. For a fixed value of α Eq. 37 is integrated and the value of Δ_{cr} is sought for which a unique solution of the wall gradient $\varphi_\chi(0)$ exists. The integration is from the wall ($\chi = 0$) up to a suitably large value of χ (typically 20), where $\varphi_\chi = 0$ according to the second boundary condition of Eq. 38. The insert of Fig. 7 provides plots of $\varphi_\chi(0)$ versus Δ_{cr} for three different values of α and the corresponding ignition Damköhler numbers Δ^*_{cr}. The plot of Δ^*_{cr} versus α is presented in Fig. 7. We further consider a propane–oxygen–nitrogen mixture with inlet composition $Y_{C3H8} = 0.0332$, $Y_{O2} = 0.3764$ (equivalence ratio $\varphi = 0.32$), and $Y_{N2} = 0.5904$ respectively. The mixture composition is the same with the chemically frozen limit example of Fig. 2. The incoming temperature is $T_{IN} = 600$ K, the pressure atmospheric, $q = 4.64 \times 10^4$ kJ/kgFuel, $W_F = 44$ kg/kmol, $W_O = 32$ kg/kmol, $\bar{W} = 29.4$ kg/kmol, $\nu_O = 5$, $c_p = 1.29$ kJ/kgK, $Pr = 0.7$, and $Le = 1.828$. A first-order reaction with respect to both the propane and oxygen is considered, of the type $B[C_{C3H8}][C_{O2}] \exp(-E/RT)$. Although the general applicability of one-step hydrocarbon reactions is questionable [34, 35], such reactions have been proposed for propane with activation energies ranging from 1.256×10^5 to 1.675×10^5 kJ/kmol [34, 36]. To be consistent with the large activation energy formulation, we use the highest value $E = 1.675 \times 10^5$ kJ/kmol and adjust the preexponential factor B to 8×10^{12} $m^3/(kmol \cdot sec)$ so that the resulting reaction rate is equal to the global reaction rate (with fractional propane and oxygen orders) proposed for flame applications [34], at about 1400 K. The specific reaction parameters are not as important for the present study, since the following results are not necessarily meant to

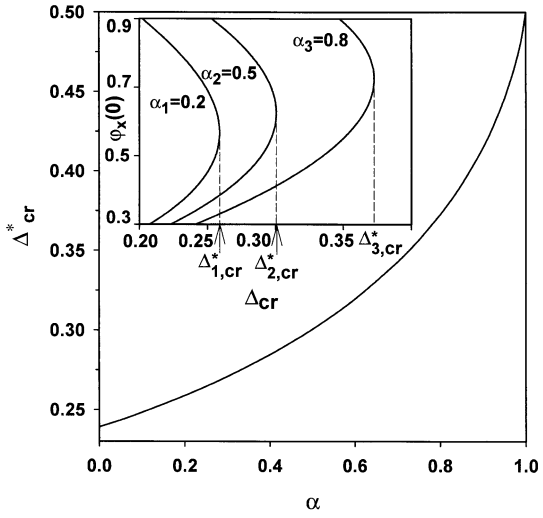

Fig. 7. Critical ignition Damköhler number Δ^*_{cr} versus α. In the insert, $\varphi_\chi(0)$ is plotted versus Δ_{cr} for three different values of α.

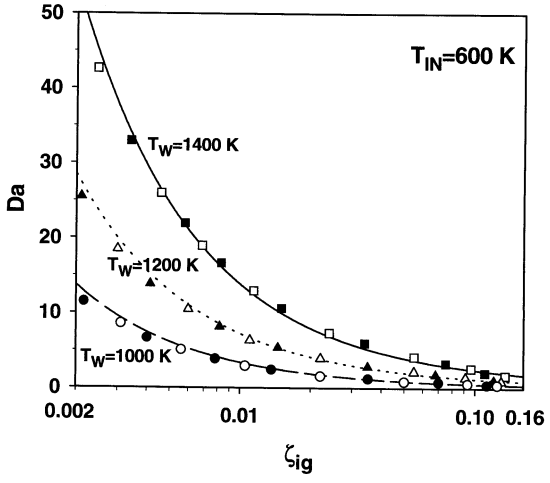

Fig. 8. Nondimensional ignition distances versus Damköhler number for fuel-lean (equivalence ratio 0.32) propane–oxygen–nitrogen mixture with T_{IN} = 600 K. Analytical results (Eq. 44) are shown for T_W = 1400 K (solid lines), T_W = 1200 K (dotted lines), and T_W = 1000 K (dashed lines). Direct numerical simulations also shown for U_{IN} = 8 m/s (solid symbols) and U_{IN} = 16 m/s (open symbols); T_W = 1400 K (squares), T_W = 1200 K (triangles), T_W = 1000 K (circles).

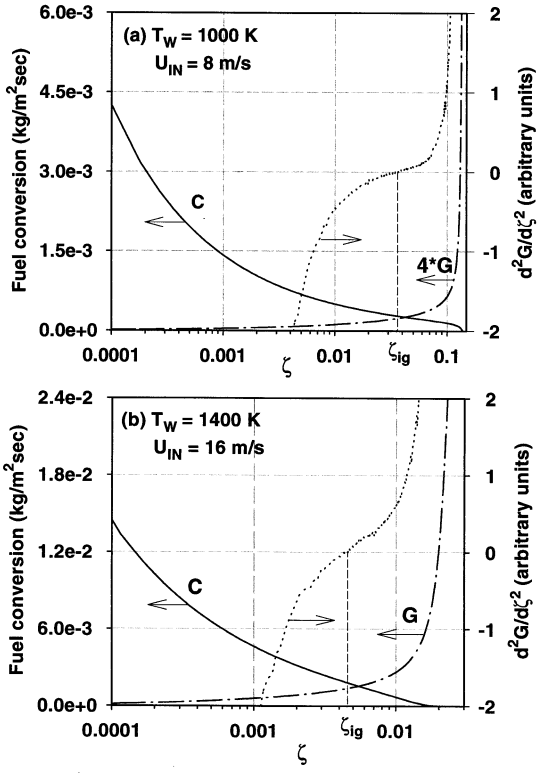

Fig. 9. Streamwise profiles of computed catalytic (C) and gaseous (G) fuel conversion. The volumetric G rate has been integrated over the channel halfwidth. The onset of homogeneous ignition defined by inflection point of the G profile. (a) T_W = 1000 K, U_{IN} = 8 m/s, T_{IN} = 600 K, b = 8.3 mm. For clarity the G profile has been expanded by a factor of four. (b) T_W = 1400 K, U_{IN} = 16 m/s, T_{IN} = 600 K, b = 2.5 mm.

provide accurate ignition distances but rather to test the functional dependencies of Eq. 44. In any case, for propane CST a minimum three-step reaction mechanism was found essential by Bruno et al. [13] to reproduce their experimental results.

Nondimensional ignition distances are plotted versus Damköhler number in Fig. 8 for three different wall temperatures, T_W = 1400 K, 1200 K, and 1000 K. It is noted that the application parameters are such that Eq. B.7 yields $\alpha < 1$, in accordance with Fig. 7. The lines in Fig. 8 are predictions from Eq. 44. It is seen that for a fixed wall temperature an increase in Da decreases the nondimensional ignition distance. The physical ignition distance also decreases, since a fixed T_W leads to a fixed chemical time and hence the diffusion time must increase: the channel halfwidth b also increases. The decrease in ζ overtakes the increase in b and the physical distance $x = \zeta bRePr$ decreases. This will be also discussed in Fig. 11 where physical ignition distances are presented. In the parametric studies of Fig. 8 the channel halfwidth b spanned the range 0.64 mm to 26 mm. Direct numerical simulations verified the functional dependence of Eq. 44. The set of Eqs. 14–20 is solved with the proposed one-step reaction and the same constant values of c_p, Pr, and Le. The solution procedure is the same as the one outlined in the chemically frozen state (see Appendix A). The definition of homogeneous ignition in the numerical simulations is illustrated in Fig. 9. In Fig. 9a the local catalytic (C) and gaseous (G) fuel conversion rates are plotted versus streamwise distance for T_W = 1000 K, b = 8.3 mm, and U_{IN} = 8 m/s (Re = 1320), while in Fig. 9b for a case with T_W = 1400 K, b = 2.5 mm, and U_{IN} = 16 m/s (Re = 794). The volumetric gaseous conversion rate has been integrated over the channel halfwidth so that it could be directly compared to the catalytic surface rate. The catalytic conversion is the highest at the channel entrance where the

mass transport coefficients are the highest and drops downstream, due to reduced mass transport coefficients and upstream fuel depletion. The gaseous fuel conversion rate increases very slowly and after a certain streamwise distance it exhibits a nearly exponential rise.

The onset of homogeneous ignition in Fig. 9 is defined as the inflection point of the G profile ($d^2G/d\zeta^2 = 0$). This definition provides ignition distances at the base of the sharp G rise (see Figs. 9a and 9b), a region where the basic approximations of the mathematical formulation are likely to hold, since in the sharp rise zone the asymptotic analysis breaks down. The presence of an inflection point in the G profile can be explained by the competition between the fuel depletion and the temperature rise. The rate of increase in the G profile ($dG/d\zeta$) drops initially as the near-wall fuel depletion increases with streamwise distance (see the transverse fuel profiles of Fig. 2a) and at the same time the mixture heating is not yet significant. As the thermal effects, however, become important the Arrhenius exponential dominates and $dG/d\zeta$ increases again. The computed ignition distance in Fig. 9a is $\zeta_{ig} = 0.0352$ ($x = 26.9$ cm) and the theoretical one from Eq. 44 is $\zeta_{ig} = 0.0334$ ($x = 25.6$ cm). In Fig. 9b the computed distance was $\zeta_{ig} = 0.00451$ ($x = 0.63$ cm) and the theoretical one is $\zeta_{ig} = 0.00466$ ($x = 0.65$ cm). Extensive numerical simulations varied b, U_{IN}, and T_W. Results are presented in Fig. 8 for two velocities; $U_{IN} = 8$ m/s (solid symbols) and $U_{IN} = 16$ m/s (open symbols). The agreement between the analytically and numerically predicted ignition distances is very good in all the cases examined. The nondimensional plot of Fig. 8 includes all the dependencies of the ignition distance on the geometrical, flow, transport, and chemical parameters of the confined configuration. It is useful, however, to extract some specific dependencies in a more direct way.

Effect of Flow Confinement

The effect of flow confinement (finite b) will be examined by comparing ignition distances to the corresponding ones of the unconfined (flat plate) case. The flat plate problem lacks a characteristic length scale and hence the proper nondimensional distance is $x/(U_{IN}\tau_{ch})$. In terms of this new distance, the confined flow solution of Eq. 44 becomes, with the aid of Eqs. 23, 41, and 45,

$$\frac{x_{ig}}{U_{IN}\tau_{ch}} = A\,\frac{\Delta^*_{cr}(\zeta_{ig})}{2PrF(\zeta_{ig})}. \tag{46}$$

As discussed in the chemically frozen limit section, the flat plate solution can be calculated with reasonable accuracy by taking the limit $\zeta \to 0$. The proper flat plate wall gradients stated in this section are, nevertheless, used resulting in (see also [21])

$$\frac{x_{ig}}{U_{IN}\tau_{ch}} = A\Delta^*_{cr}\,\frac{[f''(0)]^2}{2Sc^{1/3}}, \tag{47}$$

with the understanding that in the flat plate case of Eq. 47 the inlet properties represent free stream properties. Ignition distances $x_{ig}/(U_{IN}\tau_{ch})$ calculated from Eq. 46 are plotted in Fig. 10 versus ζ_{ig} for $T_{IN} = 400$ K and parameter T_W. In the same figure the horizontal lines indicate the corresponding flat plate solution of Eq. 47. The flat plate solution is approached as ζ_{ig} decreases. The distances $x_{ig}/(U_{IN}\tau_{ch})$ are always larger in the confined case due to the increased catalytic fuel consumption (larger surface-to-volume ratio). For a fixed T_W the confined ignition distance increases monotonically with increasing ζ_{ig}. In addition, the ratio between the confined and the unconfined ignition distances increases significantly with increasing

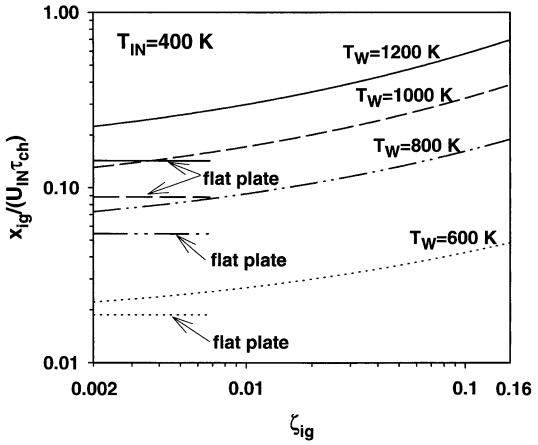

Fig. 10. Effect of flow confinement on ignition distances. Nondimensional ignition distances $x_{ig}/U_{IN}\tau_{ch}$ from Eq. 46. Horizontal lines indicate the corresponding flat plate solution of Eq. 47; $T_{IN} = 400$ K, $T_W = 600$ K (dotted lines), 800 K (dashed-dotted lines), 1000 K (dashed lines), and 1200 K (solid lines).

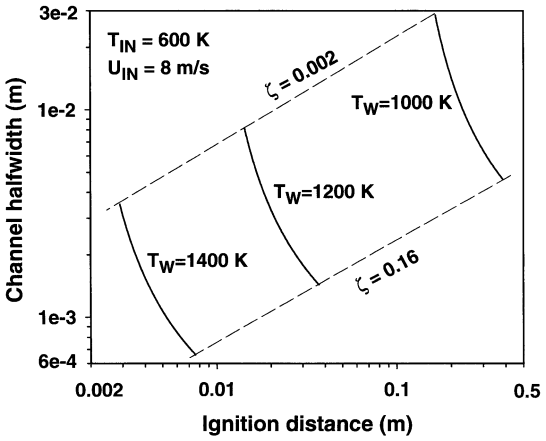

Fig. 11. Dependence of physical ignition distance on channel halfwidth for three wall temperatures. Predictions from Eq. 44, $T_{IN} = 600$ K, $U_{IN} = 8$ m/s.

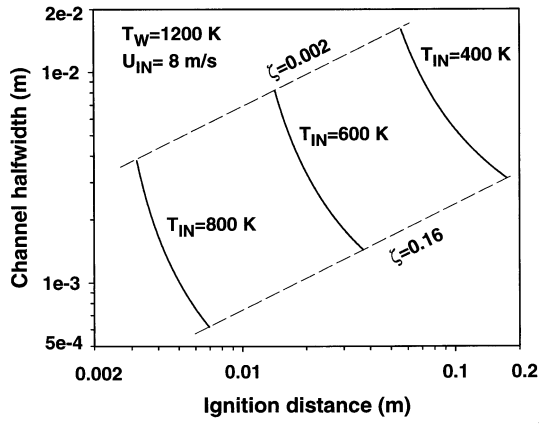

Fig. 12. Dependence of physical ignition distance on channel halfwidth for three inlet temperatures. Predictions from Eq. 44, $T_W = 1200$ K, $U_{IN} = 8$ m/s.

T_W. For example, when $T_W = 600$ K this ratio is 1.18 for $\zeta_{ig} = 0.002$ and 2.60 for $\zeta_{ig} = 0.16$. The corresponding values for $T_W = 1200$ K are 1.56 and 4.88 respectively. Hence, flow confinement is important already from $\zeta = 0.002$.

The flow confinement of the foregoing discussion is also illustrated in Fig. 11, where physical ignition distances are plotted for $T_{IN} = 600$ K and $U_{IN} = 8$ m/s. The dashed lines in this figure define the borders of applicability of Eq. 44, $\zeta = 0.002$ and $\zeta = 0.16$. For b ranging between 0.64 mm and 26 mm, the ignition distance x_{ig} ranges from 2.8 mm to 384 mm. For a fixed wall temperature the ignition distance decreases rapidly with increasing b. Although the effect of wall temperature in Eq. 44 appears through F, A, Δ^*_{cr}, and τ_{ch}, the exponential term in the chemical time scale dominates, at least for sufficiently high temperatures. This leads to a strong dependence of the ignition distance on T_W as illustrated in Fig. 11; for a fixed channel geometry with $b = 4.6$ mm, for example, an increase in the wall temperature from 1000 K to 1200 K decreases the ignition distance by a factor of 22 (from 384 mm to 18 mm).

Effect of Inlet Parameters and Transport Properties

The effect of inlet velocity U_{IN} on the ignition distance is determined from Eq. 44. For fixed b, T_{IN}, T_W, Pr, and Le the nondimensional ignition distance ζ_{ig} remains constant and hence the physical ignition distance x_{ig} is linearly proportional to the inlet velocity U_{IN} (see Eq. 23). This was also verified in the numerical simulations of Fig. 8. The open ($U_{IN} = 16$ m/s) and solid symbols ($U_{IN} = 8$ m/s) of a fixed T_W curve in Fig. 8 correspond to different channel halfwidths b. Computations with these two different (or other) velocities and the same b resulted in identical nondimensional ignition distances ζ_{ig}. The above are also consistent with recent CST measurements [16] in a channel (Pt-coated walls) with a rectangular cross section (aspect ratio 15:1) and uniform inlet velocity and temperature profiles. The homogeneous ignition distance of lean methane–air mixtures doubled with inlet velocity doubling. As evidenced from Eq. 47, the flat plate ignition distance is also proportional to the inlet velocity (see also [21]).

The effect of preheat temperature T_{IN} enters in Eq. 44 through the terms A, F, and Δ^*_{cr}. The diffusion time scale and the Reynolds number are also dependent on T_{IN}; the major influence, however, comes from the A and F terms. Physical ignition distances are plotted in Fig. 12 for $T_W = 1200$ K, $U_{IN} = 8$ m/s, for three different preheat temperatures. As seen from Fig. 12 the preheat temperature has a significant influence on the ignition distances, albeit not as strong as that of the wall temperature. With $b = 4.6$ mm, for example, an increase of the preheat temperature from 400 K to 600 K leads to a reduction of the ignition distance by a factor of six (114 mm to 18 mm).

The effect of transport parameters (Le and Pr) on the ignition distance enters in Eq. 46 (or Eq. 44) through Δ^*_{cr} and F. When Le decreases through an increase in Pr (while Sc is kept constant) the physical ignition distance always decreases. This is because Δ^*_{cr} decreases with decreasing Le, as α also decreases with decreasing Le (see Eq. B.7 and Fig. 7). When, however, Le decreases through a decrease in Sc (while Pr is kept constant), the ignition distance can either increase or decrease, depending on the specific problem parameters. This is due to the competition between Δ^*_{cr} and F in Eq. 46 as they both decrease with decreasing Le. The rate of decrease of Δ^*_{cr} is slow for small α and faster for larger α (see Fig. 7) which could lead to a ratio Δ^*_{cr}/F either increasing or decreasing with decreasing Le. Physically this can be explained as follows. The fuel depletion in the near-wall zone inhibits homogeneous ignition. As seen from Eqs. B.2 and B.5 the inner zone fuel mass fraction has two contributions. The frozen limit contribution, $\epsilon\chi\tilde{Y}_{F,IN}[(1/\tilde{Y}_{F,IN})(\tilde{Y}'_F)_{fr,W}/\theta'_{fr,W}]$, is an increasing function of Le (see Eq. 25); large Lewis numbers (small mass transport coefficients) favor homogeneous ignition as they increase the near-wall fuel levels. This effect appears in the ignition criterion of Eq. 46 through function F that includes the local wall gradient ratio. On the other hand, the weakly reactive state contribution in Eq. B.5 is (after substituting Eq. B.7 for α), $-\epsilon\varphi Le(\tilde{T}_W - \tilde{T}_{IN})$, and hence an increase in Le results in a reduction of the near-wall fuel levels. This is because once the gaseous reaction starts fuel must be replenished fast enough to sustain combustion and this is favored by small Le (large mass transport coefficients). This effect appears in the ignition criterion of Eq. 46 through Δ^*_{cr} via its dependence on α. The above described competition (also present in the flat plate case of Eq. 47) determines the net effect of Le on the ignition distance. In the application of this study, for example, when $Pr = 0.7$, $T_W = 1200$ K, and $T_{IN} = 400$ K, the ignition distance decreases by about 16% when Le decreases from 1.828 to 1.2; for $T_W = 1200$ K and $T_{IN} = 800$ K, however, the ignition distance increases by about 6% with the same reduction in Le. This effect of Lewis number on gaseous ignition distances has not been elaborated upon in previous catalytic combustion studies. The foregoing apply equally well for $0.002 < \zeta < 0.16$, as the dependence of α and the Lewis number power-law of Eq. 43 on ζ is weak.

Finally, the heat flux at the surface is examined. For a gaseous mixture flowing over a flat plate [21] or a cylindrical surface [23] the net heat flux was found to be independent of the onset of the gas-phase reaction. This is also the case for the channel flow configuration. The heat flux at the surface is,

$$Q_W = -\lambda \left.\frac{\partial T}{\partial y}\right|_W - \rho D \left.\frac{\partial Y_F}{\partial y}\right|_W q \tag{48}$$

where the second term accounts for the catalytic heat release. Introducing in Eq. 48 the variables χ, θ as well as Eqs. 35, B.5, and B.7, the dimensionless heat flux $\tilde{Q}_W = Q_W/[\lambda_{IN}(T_W - T_{IN})/b]$ becomes,

$$\tilde{Q}_W = \frac{\theta'_{fr,W}}{\sqrt{2\zeta Pr}}\left(\frac{\alpha - 1}{\alpha}\right) \tag{49}$$

Since only the chemically frozen parameters enter in Eq. 49, the net heat flux at the surface is independent of the onset of gaseous combustion. The reasoning is the same as in the external flow studies [21, 23]; the two terms in Eq. 48 balance each other, since gaseous combustion increases the temperature resulting in a decrease of the temperature wall gradient. At the same time the fuel depletion in the gas phase results in a decrease of the wall mass flux and hence in the heat released by the catalytic reaction.

CONCLUSIONS

The gas-phase ignition of fuel-lean premixtures has been studied in a plane channel flow configuration, consisting of two catalytically-active parallel plates placed at a distance $2b$ apart and held at a fixed temperature T_W. The boundary layer approximation was employed, along with a one-step large activation energy gaseous reaction and an infinitely fast catalytic reaction. The following are the key conclusions of this study:

1. The critical Damköhler numbers for the confined flow problem were identified through a numerical solution and parametric description of the corresponding chemically frozen

state and a first-order perturbation for the weakly reactive state.

2. A closed-form implicit ignition criterion is obtained in terms of nondimensional groups that are relevant to confined flows and based on the geometrical, flow, chemical, and transport parameters. The solution is valid over the range $0.002 < x/(bRePr) < 0.16$. The temperature range of applicability is $1.5 < T_W/T_{IN} < 3.0$ and the transport parameter range is $0.6 < Pr < 1.0$ and $0.9 < Le < 2.0$. The temperature and transport parameter ranges encompass most of the hydrocarbon CST applications. In addition, the streamwise extent of applicability is significant, particularly at high-pressure CST conditions.
3. The Damköhler number of the problem (ratio of characteristic transverse diffusion time to characteristic chemical time) is included explicitly in the ignition criterion, clearly showing the competition between catalytic and gaseous fuel conversion. The effect of flow confinement (b) is included implicitly in the ignition criterion.
4. Numerical simulations were performed for channel CST of a fuel-lean (equivalence ratio of 0.32) propane–oxygen–nitrogen mixture. The analytically calculated ignition distances are in good agreement with those from the numerical predictions, providing direct verification for the functional dependence of the ignition criterion.
5. Ignition distances of the confined case are compared with the corresponding ones for the unconfined flat plate case. Ignition distances increase with decreasing plate separation and can be significantly higher than those for the unconfined case, particularly at higher T_W/T_{IN}. In addition, the effect of flow confinement is important from $x/(bRePr) = 0.002$.

APPENDIX A

Numerical Solution Procedure

The set of Eqs. 14, 21, 22, and 17 subject to the initial and boundary conditions of Eqs. 18–20 constitutes a parabolic system with dependent variables θ, q, $\tilde{Y}_i$, and p^*. For the species boundary conditions, Eq. 9 is used (equivalent to Eq. 19 when the species diffusivities are equal). Since no explicit boundary condition is provided for the pressure, an additional boundary condition is used for the normalized stream function; at the plane of symmetry ($\eta = \eta^*$) $f = 1/\sqrt{2s}$. This boundary condition is simply the conservation of total mass at any streamwise location. A reference value for one of the transport properties is also provided. Typically μ_{IN} is calculated at the inlet conditions and then its local value is computed as $\mu = \mu_{IN}\rho_{IN}/\rho$ while the other transport properties are evaluated from μ and the fixed values of c_p, Pr, and Sc. The system of differential equations are discretized using a finite difference approach. Central difference is used for both the first- and second-order derivatives. Up to 400 grid points are used in the transverse direction (with finer spacing towards the wall), sufficient to produce a grid-independent solution. The system of discretized equations forms a set of differential-algebraic equations which is solved numerically using the computer program DASSL [28]. The governing equations are written in the form

$$H\left(g, \frac{dg}{ds}, s\right) = 0 \tag{A.1}$$

with g the components of the solution and dg/ds their streamwise derivative. DASSL performs an integration in s using an implicit stepping method. The maximum local relative error is set to 10^{-5}. Marching in s provides the solution up to the desired streamwise distance.

APPENDIX B

Inner Species Expansions

The terms G_1 and $\tilde{\omega}$ in Eq. 36 are expressed for the inner region as follows. Substitution of the inner zone expression for f (given after Eq. 33) in the definition of G_1 yields $G_1 = 1 - Prf''_W\eta^3/6 \approx 1$ for $\eta \to 0$. For $\tilde{\omega}$ (see Eq. 29) the term $(1 - \beta\theta)$ with the use of Eq. 35 becomes $1 + \epsilon\beta(\varphi - \chi) \approx 1$, neglecting the $O(\epsilon)$ contribution. Similarly, the exponential term in Eq. 29 becomes $\exp[-\tilde{T}_a(1 - \beta\epsilon(\varphi - \chi))]$. Setting

$$\epsilon = \frac{1}{\beta \tilde{T}_a} = \frac{T_W^2 R}{(T_W - T_{IN})E}, \tag{B.1}$$

the exponential term is $\exp(-\tilde{T}_a)\exp(\varphi - \chi)$. The fuel and oxidizer mass fractions in Eq. 29 are expressed again with first-order expansions. For the fuel,

$$\tilde{Y}_{F,inr} = \tilde{Y}_{F,fr} - \epsilon\psi \tag{B.2}$$

with ψ the fuel mass fraction perturbation. The frozen limit solution near the wall is

$$\tilde{Y}_{F,fr} = \tilde{Y}_{F,W} + (\tilde{Y}'_F)_{fr,W}\eta + O(\eta^2) = (\tilde{Y}'_F)_{fr,W}\eta, \tag{B.3}$$

since $\tilde{Y}_{F,W} = 0$. The temperature and fuel mass fraction perturbations φ and ψ can be related as

$$\psi = \varphi\alpha[(\tilde{Y}'_F)_{fr,W}/\theta'_{fr,W}] \tag{B.4}$$

with α to be determined in the following. Substitution of Eqs. B.3 and B.4 to B.2 and using Eq. 34 yields the inner solution for the fuel mass fraction

$$\tilde{Y}_{F,inr} = \epsilon(\chi - \alpha\varphi)\tilde{Y}_{F,IN}\left[\frac{(1/\tilde{Y}_{F,IN})(\tilde{Y}'_F)_{fr,W}}{\theta'_{fr,W}}\right]. \tag{B.5}$$

Note that the bracket in Eq. B.5 involves the transverse wall gradient ratio determined in the chemically frozen limit section (Eq. 25).

The equivalent to Eq. 31 conservation equation for the fuel mass fraction is then constructed, Eq. B.5 is substituted in it, and the leading term in ϵ balancing the reaction term is kept, resulting in

$$\frac{d^2\varphi}{d\chi^2} = -\frac{\epsilon Sc2s\tilde{B}\tilde{\omega}}{G_1^2\theta'_{fr,W}(\tilde{Y}'_F)_{fr,W}\alpha} \tag{B.6}$$

with the same boundary conditions as that of Eq. 36. Comparison of Eqs. 36 and B.6 reveals that $\alpha = Le\beta\tilde{T}_W[\theta'_{fr,W}/(\tilde{Y}'_F)_{fr,W}]$ and substituting β from Eq. 26,

$$\alpha = \frac{Le(\tilde{T}_W - \tilde{T}_{IN})}{\tilde{Y}_{F,IN}}\left[\frac{\theta'_{fr,W}}{(1/\tilde{Y}_{F,IN})(\tilde{Y}'_F)_{fr,W}}\right]. \tag{B.7}$$

The parameter α expresses the influence of the thermal to the mass diffusion ratio on gaseous ignition. First-order expansion is also carried out for the oxidizer. In a similar procedure to that of Eqs. B.2–B.5 for the fuel, the inner solution for the oxidizer is, $\tilde{Y}_{O,inr} = \tilde{Y}_{O,W} + \epsilon(\chi - \alpha\varphi)\tilde{Y}_{F,IN}[(1/\tilde{Y}_{F,IN})(\tilde{Y}'_F)_{fr,W}/\theta'_{fr,W}]$ and using Eq. 19 for $\tilde{Y}_{O,W}$,

$$\tilde{Y}_{O,inr} = (\tilde{Y}_{O,IN} - \tilde{Y}_{F,IN}) + \epsilon(\chi - \alpha\varphi)\tilde{Y}_{F,IN}\left[\frac{(1/\tilde{Y}_{F,IN})(\tilde{Y}'_F)_{fr,W}}{\theta'_{fr,W}}\right]. \tag{B.8}$$

When there is sufficient excess of oxidizer (which is the case in CST applications), $(\tilde{Y}_{O,IN} - \tilde{Y}_{F,IN}) \gg \epsilon\tilde{Y}_{F,IN}[(1/\tilde{Y}_{F,IN})(\tilde{Y}'_F)_{fr,W}/\theta'_{fr,W}]$, resulting in

$$\tilde{Y}_{O,inr} = \tilde{Y}_{O,IN} - \tilde{Y}_{F,IN}. \tag{B.9}$$

Substitution of Eqs. 28, B.1, B.5, B.9, the value of G_1, and the Arrhenius exponential term described in the beginning of this Appendix into the perturbation Eq. 36 leads to Eqs. 37–39.

Support for this work was provided by the Swiss Federal Office of Energy (BFE) under contract No. 59048.

REFERENCES

1. Stambler, I., *Gas Turbine World* 23:3 (1993).
2. Schlegel, A., Buser, S., Benz, P., Bockhorn, H., and Mauss, F., *Twenty-Fifth Symposium (International) on Combustion*, The Combustion Institute, Pittsburgh, 1994, pp. 1019–1026.
3. Schlegel, A., Benz, P., Griffin, T., Weisenstein, W., and Bockhorn, H., *Combust. Flame* 105:332–340 (1996).
4. Song, X., Williams, W. R., Schmidt, L. D., and Aris, R., *Twenty-Third Symposium (International) on Combustion*, The Combustion Institute, Pittsburgh, 1990, pp. 1129–1137.
5. Song, X., Williams, W. R., Schmidt, L. D., and Aris, R., *Combust. Flame* 84:292–311 (1991).
6. Ikeda, H., Libby, P. A., Williams, F. A., and Sato, J., *Combust. Flame* 93:138–148 (1993).
7. Bui, P. A., Vlachos, D. G., and Westmoreland, P. R., *Twenty-Sixth Symposium (International) on Combustion*, The Combustion Institute, Pittsburgh, 1996, pp. 1763–1770.
8. Schefer, R. W., *Combust. Flame* 45:171–190 (1982).
9. Griffin, T. A., Pfefferle, L. D., Dyer, M. J., and Crosley, D. R., *Combust. Sci. Technol*. 65:19–37 (1989).
10. Markatou, P., Pfefferle, L. D., and Smooke, M. D., *Combust. Sci. Technol*. 79:247–268 (1991).
11. Markatou, P., Pfefferle, L. D., and Smooke, M. D., *Combust. Flame* 93:185–201 (1993).
12. Buser, S., Benz, P., Schlegel, A., and Bockhorn, H., *Ber. Bunsenges. Phys. Chem*. 97:1719–1723 (1993).
13. Bruno, C., Walsh, P. M., Santavicca, D. A., Sinha, N.,

Yaw, Y., and Bracco, F. V., *Combust. Sci. Technol*. 31:43–74 (1983).
14. Bruno, C., Walsh, P. M., Santavicca, and Bracco, F. V., *Int. J. Heat Mass Transfer* 26:1109–1120 (1983).
15. Dogwiler, U., Benz, P., and Mantzaras, J., *Combust. Flame* 116:243–258 (1999).
16. Dogwiler, U., Mantzaras, J., Benz, P., Kaeppeli, B., Bombach, R., and Arnold, A., Twenty-Seventh Symposium (International) on Combustion, The Combustion Institute, Pittsburg, 1998, pp. 2275–2282.
17. Deutschmann, O., Schmidt, R., Behrendt, F., and Warnatz, J., *Twenty-Sixth Symposium (International) on Combustion*, The Combustion Institute, Pittsburgh, 1996, pp. 1747–1754.
18. Law, C. K., and Sivashinsky, G. S., *Combust. Sci. Technol*. 29:277–286 (1982).
19. Law, C. K., and Chung, S. H., *Combust. Sci. Technol*. 32:307–312 (1983).
20. Trevino, C., *Combust. Sci. Technol*. 30:213–229 (1983).
21. Trevino, C., and Fernandez-Pello, A. C., *Combust. Sci. Technol*. 26:245–251 (1981).
22. Trevino, C., and Peters, N., *Combust. Flame* 61:39–49 (1985).
23. Rangel, R. H., Fernandez-Pello, A. C., and Trevino, C., *Combust. Sci. Technol*. 48:45–63 (1986).
24. Langhaar, H-L., *J. Appl. Mech*. ASME 64:A-55 (1942).
25. Han, L. S., *J. Appl. Mech*. ASME 82:403–409 (1960).
26. Sparrow, E. M., Lin, S. H., and Lundgren, T. S., *Phys. Fluids* 73:338–347 (1964).
27. Williams, F. A., *J. Fluid Mech*. 34:241–261 (1968).
28. Brenan, K. E., Campbell, S. L., and Petzold, L. R., *Numerical Solution of Initial Value Problems in Differential-Algebraic Equations*, North-Holland, New York, 1989.
29. Kays, W. M., and Crawford, M. E., *Convective Heat and Mass Transfer*, 2nd ed., McGraw-Hill, New York 1980.
30. Schlichting, H., *Boundary Layer Theory*, McGraw Hill, New York, 1979, p. 294.
31. Jones, C. W., and Watson, E. J., in *Laminar Boundary Layers* (L. Rosenhead, Ed.), Dover Publications, New York, 1988, p. 224.
32. Hwang, C. L., in *Laminar Flow Forced Convection in Ducts* (R. K. Shah and A. L. London, Eds.), Academic Press, New York, 1978, p. 191.
33. Law, C. K., and Law, H. K., *J. Fluid Mech*. 92:97–108 (1979).
34. Westbrook, C. K., and Dryer, F. L., *Combust. Sci. Technol*. 27:31–43 (1981).
35. Coffee, T. P., Kotlar, A. J., and Miller, M. S., *Combust. Flame* 54:155–169 (1983).
36. Puri, I. K., and Seshadri, K., *Combust. Flame* 65:137–150, (1986).

Received 7 December 1998; revised 18 May 1999; accepted 23 May 1999